SKA memo 103, 14 aug 2008

Deconvolving Primary Beam Patterns from SKA Images

Melvyn Wright & Stuartt Corder

University of California, Berkeley, & Caltech, Pasadena, CA.

ABSTRACT

In this memo we present a method for deconvolving the primary beam response from interferometric images of astronomical sources. The measured primary beam may be time variable, non axi-symmetric and different at each station in the interferometer array. The method is a simple extrapolation of existing software which subtracts a model of the sky brightness distribution from *uv* data. After subtracting the best estimate of the sky brightness distribution weighted by the measured primary beam pattern, the residual *uv* data can be re-imaged to provide an improved model of the sky brightness distribution and the process iterated if needed until the residual *uv* data are consistent with thermal noise and residual instrumental errors. The data are imaged using canonical, time invariant primary beam patterns, and deconvolved using the measured primary beam voltage patterns for each station.

In this memo we simulate observations with the heterogeneous CARMA telescope and calculate the errors which result from the measured primary beam voltage patterns. We show that the effects of the measured $\sim$ 1 - 5% deviations from the canonical beam patterns can be devastating, reducing the image fidelity from $\sim$ 8000 to $\sim$ 50 for a source which fills the primary beam FWHM. The image fidelity can be greatly improved by using the measured voltage patterns in the deconvolution.

The primary beam pattern is the product of the voltage patterns for each station pair, and is complex valued if the voltage patterns are not identical. This results in a complex valued image of a real, total intensity, sky brightness distribution; i.e. the image shows a polarized flux distribution which varies across the primary beam, and any real polarization distribution is confused by flux scattered from the total intensity by primary beam errors. Polarization images can be corrected by subtracting a model of the source weighted by the complex valued primary beam patterns from the *uv* data.

1. Introduction

An aperture synthesis array samples the cross correlation of the signals from an array of antennas, or phased array stations in the case of the SKA. The signal from each station measures the sky brightness distribution weighted by the voltage pattern of the phased array at each station.

Images of the sky brightness are formed by combining the measured cross correlations between the stations. The usual assumption for aperture synthesis imaging is that the illumination of the sky by the primary beam pattern is invariant, and the same for all stations, then an image of the primary beam weighted sky brightness can be formed from a Fourier transform of the measured cross correlations. Sources larger than the primary beam require a mosaic of interferometer and single dish observations at multiple pointing centers.

For a point source at the pointing center, e.g. a quasar calibration observation, the array response is well described by the forward gain. For an extended source distribution, the array response depends on the primary beam illumination of the sky for each station pair.

The effects of amplitude and phase errors in the calibration of the measured cross correlations are well known. Less well appreciated are the pernicious effects of amplitude and phase errors in the primary beam illumination of an extended source distribution. The case for a homogeneous array of antennas has been well studied. The image fidelity for mosaic observations is limited by pointing and primary beam errors (Cornwell, Holdaway & Uson, 1993; Holdaway, 1998).

In this memo we simulate observations with the CARMA telescope and calculate the errors which result from the measured primary beam voltage patterns. These results are relevant to all aperture synthesis arrays, including millimeter/submillimeter wavelength arrays like ALMA, and cm/m wavelength arrays like ATA and SKA.

The SKA will be a heterogeneous telescope with different primary beam patterns for each antenna station. The CARMA telescope is a heterogeneous array, with six 10.4 m, and nine 6.1 m antennas. The different antenna diameters and primary beam sizes allow regions up to $\sim 32''$ diameter to be observed with a single pointing center. Regions up to $\sim 64''$ diameter can be observed with a 7-pointing hexagonal mosaic. Because of the different primary beam patterns, imaging with a heterogeneous array must be treated as a mosaic observation even when only a single pointing center is used for all antennas. (Carma memo 38).

The FWHM at 100 GHz is given in Table 1 assuming a Gaussian primary beam pattern for each antenna. Images can be made from a mosaic of pointing centers by using the three primary beam types in Table 1. (see Sault, Staveley-Smith and Brouw, 1996, and the MIRIAD Users Guide for a more extensive discussion). However, if proper account is not taken of the different primary beam response for each antenna pair, amplitude and phase errors in the measured cross correlations on different interferometer baselines degrade the image fidelity.

We show that the effects of the measured ~ 1 - 5% deviations from the canonical beam patterns can be devastating, reducing the image fidelity from ~ 8000 to ~ 50 for a source which fills the primary beam FWHM. The image fidelity can be greatly improved by using the measured voltage patterns in the deconvolution. We present a method for deconvolving the primary beam response from interferometric images of astronomical sources.

2. Mosaicing Simulations

We simulated observations using an image of Cas A scaled to different diameters as a source model. Simulated *uv* data sampled by the heterogeneous array of 10.4, and 6.1 m antennas were used to make images at 100 GHz for the compact D-configuration of the CARMA 15- antenna array. Figure 1 shows the VLA Image model of Cas A scaled to 128″ diameter. *uv* data were generated from the model image. Thermal noise was added to the *uv* data using a double sideband receiver temperature 80 K and a zenith opacity 0.26 at 100 GHz. We used a bandwidth 4 GHz and the antenna gains listed in Table 1 assuming an aperture efficiency 75% . The *uv* data were sampled from -2 to +2 hours which gives good azimuthal *uv* coverage and minimizes antenna shadowing (CARMA memo 5). Amplitude calibration errors were simulated by multiplying the *uv* data by random gain variations for each antenna on a 30 min time scale, commensurate with the typical calibration interval. The thermal noise in the image for each sub-array is listed in Table 1.

We generated the *uv* data for a mosiac with a single pointing center and a single linear polarization feed (MIRIAD: uvgen). We made images using the standard MIRIAD software (invert, mosmem) using the Gaussian beams listed in Table 1. The images were deconvolved using both the canonical Gaussian primary beams, and the measured primary beams. The primary beam pattern is the product of the voltage patterns for each antenna pair, and is complex valued if the voltage patterns are not identical. We used the measured voltage patterns (Corder & Wright, 2006) to generate the real and imaginary parts of the primary beam pattern for each antenna pair, and used these to generate *uv* data corresponding to the image model illuminated by the measured primary beam patterns.

The measured primary beams may be time variable, non axi-symmetric and different on each antenna in the interferometer array. The data are imaged using canonical, time invariant primary beam patterns, and deconvolved using the measured primary beam voltage patterns for each antenna. The method is a simple extrapolation of existing software which subtracts a model of the sky brightness distribution from the *uv* data. After subtracting the best estimate of the sky brightness distribution weighted by the measured primary beam pattern, the residual *uv* data can be re-imaged to provide an improved model of the sky brightness distribution and the process iterated if needed, until the residual *uv* data are consistent with thermal noise or other residual instrumental errors.

Table 1: CARMA Primary Beam FWHM, Gain and Thermal Noise at 100 GHz

Antennas	Equivalent diameter	FWHM	Gain	Thermal noise
m x m	m	arcsec	Jy/K	mJy
10.4 x 10.4	10.4	64	43	0.76
10.4 x 6.1	8.0	83	73	0.69
6.1 x 6.1	6.1	115	126	1.4

3. Results

Table 2 lists the results of the mosaicing simulations. In the first 3 lines a mosaic image for 3 different source diameters was deconvolved using the Maximum Entropy (MEM) algorithm (MIRIAD: mosmem) with the canonical Gaussian primary beams. The image fidelity was calculated from the difference between the MEM image and the original image model convolved to the same resolution by a Gaussian restoring beam. The MEM deconvolutions used the interferometer data with a total flux constraint. Single dish data were not included in this simulation. The image fidelity is listed in the last column as the ratio of the peak flux density in the model to the on-source RMS in the residual image. The image fidelity increases as the source size decreases from $128''$ to $32''$ reflecting the better uv sampling for the smaller source diameter.

Much higher image fidelity is obtained by deconvolving in the uv domain. After subtracting the model image weighted by the canonical Gaussian primary beams the residual uv data are re-imaged. Table 2 lists the results for a source diameter $128''$ and $64''$. For a $64''$ source diameter, the image fidelity approaches the theoretical noise level. For a $128''$ source diameter, the image fidelity again reflects the poorer uv sampling for the larger source.

Using the measured measured primary beam voltage patterns for each antenna we can subtract the model image weighted by the actual primary beams for each antenna pair. Both real and imaginary parts of the primary beam must be subtracted. Table 2 lists the resulting image fidelity obtained when the actual primary beams are substituted for the canonical Gaussian primary beams for various antenna pairs. The resulting image fidelity is much poorer. The modeling is actually the reverse of real observations where the uv data are generated with the real primary beam patterns, and deconvolved using Gaussian primary beam models, but the residual image shows the difference in both cases. The RMS on the residual image, and the resulting image fidelity varies greatly with the antenna pair used. This is a consequence of both the primary beam illumination of the source distribution, and the spatial frequencies sampled by the antenna pair. The Cas A model image used in these simulations has a fractal-like structure with a wide range of spatial frequencies over the whole image, which minimizes the effects of the spatial frequencies sampled by each antenna pair. Antennas 1 and 5, both 10m antennas, have large deviations from the Gaussian model and give large residuals and lower image fidelity. Antennas 2 and 3, also 10m antennas, have smaller deviations from the Gaussian model and give smaller residuals. Antenna pairs including 6m antennas generally have small deviations from the Gaussian model and give higher image fidelity.

Table 2 lists the image fidelity using the measured primary beam voltage patterns for all antennas for 3 different source diameters. Although both real and imaginary parts of the primary beam must be subtracted, using only the real part already degrades the image fidelity for a $128''$ source diameter from 8062 to 53. Including the imaginary part of the primary beam reduces the image fidelity to 41. For a $64''$ source diameter the image fidelity is even lower. This somewhat counter intuitive result can be understood when it is realized that the primary beam errors are only important if they illuminate the source distribution. For a $128''$ source diameter, a large part the

the source is not illuminated by the errors in the 10m antenna primary beams for a single pointing centered on the Cas A model image. For $32''$ and $16''$ source diameters the image fidelity increases as the source is illuminated by the inner parts of the primary beam patterns which have smaller errors.

4. Discussion

4.1. Errors in the uv data from primary beam errors

These results can be understood in terms of the errors in the uv data induced by errors in the primary beam patterns. Figure 1 shows the VLA image model of Cas A scaled to $128''$ diameter. Figure 2 shows the mosaic image of the Cas A model using a single pointing center at an observing frequency 100 GHz. The grey scale pixel image shows the maximum entropy deconvolution using the three standard truncated Gaussian primary beam models for 10m-10m 10m-6m and 6m-6m antenna pairs. The contours show the residual image when the measured voltage patterns for just one antenna pair, antennas 1 and 8, is used instead of the truncated Gaussian model. The errors in the image are very similar to amplitude and phase calibration errors of the uv data, but in this case are caused by amplitude and phase errors in the primary beam illumination of the source.

Figure 3 shows the primary beam pattern for cross correlation between antennas 2 and 6. The real part of the complex primary beam is similar to the canonical Gaussian model, but the imaginary part shows an asymmetric gradient caused by an offset illumination of the aperture on this pair of antennas.

Figure 4 shows the amplitude of uv data with antennas 2 and 6. Black points are the simulated uv data. The red curve is the model visibility for the Gaussian model primary beam pattern used to generate the uv data. The blue curve is the model visibility using the real part of the measured primary beam response. The green curve is the model visibility using both the real and imaginary parts of the measured primary beam response. Figure 5 shows the phase of the uv data. The amplitude and phase errors in the measured the uv data are caused by amplitude and phase errors in the primary beam illumination of the source. Figure 6 shows the primary beam pattern for cross correlation between antennas 7 and 9. Here the deviations from the Gaussian model primary beam are much smaller and the corresponding amplitude and phase errors in the measured uv data are much smaller (Figures 7 & 8).

The primary beam pattern is the product of the voltage patterns for each antenna pair. Cross correlations between 6 and 10m antennas are in some cases poorly represented by the corresponding Gaussian model, and give large amplitude and phase errors in the measured uv data (e.g. antennas 6 and 11 in Figures 9, 10, 11), and in other cases are well represented by the Gaussian model and give smaller errors in the uv data (e.g. antennas 2 and 11 in Figures 12, 13, 14). Detailed inspection of the results for these antenna pairs is quite instructive in understanding the effects of

errors in the real and imaginary parts of the primary beam patterns.

Pointing errors also cause amplitude and phase errors in the measured *uv* data by changing the illumination pattern of the source. In these simulations the effects of pointing errors have been removed by centering the measured voltage patterns, since pointing errors can be corrected on line before acquiring the observations. The measured deviations in the primary beam patterns are not well represented by focus errors although focus corrections are not currently made on-line.

4.2. Polarization errors

The primary beam pattern is the product of the voltage patterns for each antenna pair, and is complex valued if the voltage patterns are not identical. This results in a complex valued image of a real, total intensity, sky brightness distribution; i.e. the image shows a polarized flux distribution which varies across the primary beam, and any real polarization distribution is confused by flux scattered from the total intensity by primary beam errors.

We investigated the magnitude of the polarization errors by generating *uv* data from the Cas A image weighted by the imaginary part of the measured primary beam response for each antenna pair. The *uv* data were sampled from -2 to +2 hours with the primary beam rotated to the correct paralactic angle at 0.5 hour intervals.

The *uv* data were then imaged. The imaginary part of the image, which should be zero for a real sky brightness distribution, contains the instrumental polarization response which results from the illumination of the total intensity distribution by the imaginary part of the measured primary beam patterns.

Figure 15 shows the polarization errors which would be observed in position angle zero. The peak to peak signal $\sim$ -0.7 to 0.7 Jy with an RMS $\sim$ 150 mJy. Sampling multiple paralactic angles dilutes the errors since the primary beam error pattern rotates on the sky. When only one paralactic angle was sampled, the error pattern in the image was more pronounced, but did not significantly change the RMS value. The instrumental polarization response across the primary beam has an RMS $\sim$ 4%, with peak values +/– 20% of the peak in the total intensity image.

Polarization images can be corrected for the measured primary beam patterns in the same way that we created the model errors above; i.e. by subtracting a model of the total intensity image weighted by the complex valued primary beam patterns from the measured *uv* data. The polarization image is limited by the image fidelity of the total intensity model and by errors in the measured primary beam patterns. For strongly polarized sources a more rigorous treatment of calibration in terms of 2x2 Jones and coherency matrices can be used to avoid polarization distortion of the Stokes parameters. (see Hamaker, 2000)

The instrumental polarization response across the primary beam can be significantly improved by reducing the imaginary part of the primary beam response which arises from asymmetries in

the aperture illumination. Figure 16 shows the instrumental polarization response to the Cas A total intensity model when the primary beam voltage pattern for one of the 10m antennas with a large offset aperture illumination is replaced by one with a more symmetric pattern. As can be seen from the examples we provided, antenna 6 has a large phase gradient across the primary beam resulting from an offset aperture illumination. However, the largest primary beam errors come from the antenna pair 1–4 which have a gradient in the same direction, so together they have a large polarization response across the primary beam. Figure 16 shows the instrumental polarization across the Cas A image when the voltage pattern for antenna 1 is corrected to the errors measured in antenna 3. The resulting instrumental polarization response is significantly improved.

5. Conclusion

In this memo we simulate observations with the CARMA telescope and calculate the image errors which result from the measured primary beam voltage patterns at 100 GHz. These results are relevant to all aperture synthesis arrays, including millimeter/submillimeter wavelength arrays using standard antennas like ALMA, and cm/m wavelength arrays like ATA and SKA. The results are especially relevant for aperture arrays on the SKA where the nominal primary beam is highly varying. The image fidelity can be greatly improved by using the measured voltage patterns in the deconvolution.

The primary beam pattern is the product of the voltage patterns for each pair of antenna stations, and is complex valued if the station voltage patterns are not identical. This results in a complex valued image of a real, total intensity, sky brightness distribution; i.e. the image shows a polarized flux distribution which varies across the primary beam. The total intensity image is degraded, and any real polarization distribution is confused by flux scattered from the total intensity by primary beam errors. A corollary is that a full polarization measurement is needed to correct the total intensity image across the primary beam.

Images can be corrected by subtracting a model of the source weighted by the complex valued primary beam patterns for each antenna station pair from the *uv* data. Errors in the model of the sky brightness distribution, and in the measured voltage patterns for each antenna station determine the errors in the corrected *uv* data. After subtracting the best estimate of the sky brightness distribution weighted by the measured primary beam pattern, the residual *uv* data can be re-imaged to provide an improved model of the sky brightness distribution and the process iterated if needed, until the residual *uv* data are consistent with thermal noise and other residual instrumental errors.

At millimeter wavelengths, the voltage patterns may be best measured on strong astronomical sources, or with a transmitter to obtain sufficient signal to noise. If the primary beam voltage patterns can be characterized as a function of elevation, temperature etc, then these data can be used to correct the *uv* data, as we have done for CARMA.

At cm/m wavelengths, the sky brightness distribution itself may provide the best voltage patterns measurements. The problem is a self-calibration determining a sky brightness distribution and primary beam patterns which are consistent with the *uv* data in the sense that when the final model of the sky brightness distribution weighted by the primary beam patterns is subtracted, the residual *uv* data are consistent with the noise. (e.g. LOFAR calibration and imaging, Nijboer, R. J., Noordam, J. E., 2005, 2006; SKA memo 60, Wright, 2005)

On many of the CARMA 10m antennas, the real part of the complex primary beam is similar to the canonical Gaussian model, but the imaginary part shows an asymmetric gradient caused by an offset illumination of the aperture. The instrumental polarization response across the primary beam can be significantly improved by reducing the imaginary part of the primary beam response which arises from asymmetries in the aperture illumination.

Primary beam errors are present in all aperture synthesis arrays and limit the image fidelity. At some level all arrays are heterogeneous. The alignments of the antenna surface, subreflectors, and receiver feeds, feed leg blockage and reflections on the antenna structure all contribute to offsets and asymetries in the aperture illumination. The magnitude and stability of these alignments will determine how well we can correct the data for primary beam characteristics.

For a phased array station beam, atmospheric fluctuations make the complex valued station beam time variable. Even for a clean voltage pattern with low level sidelobes from a single antenna, the complex sidelobe pattern will vary with time due to pointing errors, which cause a time varying illumination of the sky brightness distribution. Although it can be argued that expensive, high precision antennas are not needed for low frequency observations, primary beam and pointing errors dominate the image errors in mosaic observations of large sources. If the antennas are engineered for observations at higher frequency, then we will have more stable primary beam illumination patterns at lower frequencies, and fewer parameters which must be determined to calibrate the data.

Table 2: Mosaicing simulations for Cas A at 100 GHz. Using single pointing mosaic with 1% gain noise. The table gives the source diameter and the image fidelity for each deconvolution method. MEM deconvolution with total flux constraint, 732.069 Jy

Method	diam[″]	Fidelity
MEM deconvolution using Gaussian PB	128	18
MEM deconvolution using Gaussian PB	64	82
MEM deconvolution using Gaussian PB	32	246
subtract Gaussian PB from *uv* data	128	8062
subtract Gaussian PB from *uv* data	64	44775
measured PB for ant 1 and 5	128	249
measured PB for ant 2 and 3	128	1294
measured PB for ant 1 and 8	128	3198
measured real PB for all antennas.	128	53
measured complex PB for all antennas.	128	41
measured complex PB for all antennas.	64	31
measured complex PB for all antennas.	32	38
measured complex PB for all antennas.	16	73

6. References

Bob Sault & Neil Killeen, 1999, *Miriad Users Guide*, http://www.atnf.csiro.au/computing/software/miriad

Corder, S., & Wright, M., 2006, *CARMA Holography*, CARMA memo 36, http://www.mmarray.org

Cornwell, T.J., Holdaway, M.A. & Uson, J.M., 1993, *Radio-interferometric imaging of very large objects: implications for array design*, A&A 271, 697.

Hamaker, Johan P. 2000, *Understanding radio polarimetry. IV. The full-coherency analogue of scalar self-calibration: Self-alignment, dynamic range and polarimetric fidelity* Astronomy and Astrophysics Supplement, 143, 515

Holdaway, M. A., 1998, *Mosaicing with Interferometer Arrays*, in Synthesis Imaging in Radio Astronomy II, ASP Conference Series, G. B. Taylor, C. L. Carilli and R. A. Perley (Eds)

Holdaway. M.A., 1999, *Mosaicing with Interferometer Arrays*, ASP Conference series 180, 401.

Nijboer, R. J., Noordam, J. E., 2005, *LOFAR Calibration*, Astronomical Data Analysis Software and Systems XVI ASP Conference Series, Vol. 376, 237, Richard A. Shaw, Frank Hill and David J. Bell. (Eds)

Nijboer, R. J., Noordam, J. E., Yatawatta, S. B., 2006, *LOFAR Self-Calibration using a Local Sky Model*, Astronomical Data Analysis Software and Systems XV ASP Conference Series, Vol. 351, 291, Carlos Gabriel, Christophe Arviset, Daniel Ponz, and Enrique Solano. (Eds)

Sault, R.J., Staveley-Smith, L & Brouw, W.N., 1996, *An approach to interferometric mosaicing*, A&A Supp., 120, 375

Wright, M.C.H., 1999, *BIMA Array response to extended structure*, BIMA memo 45, http://bima.astro.umd

Wright, M.C.H., 1999, *Image Fidelity*, BIMA memo 73, http://bima.astro.umd.edu/memo/memo.html

Wright, Melvyn, 2002, *Compact Configuration Evaluation for CARMA*, CARMA memo 5, http://www.mmarray.org

Wright, Melvyn, 2005, *Real Time Imaging*, SKA memo 60

Wright, Melvyn, 2007, *Image Fidelity as a Function of Source Size and Calibration Errors*, CARMA memo 38, http://www.mmarray.org

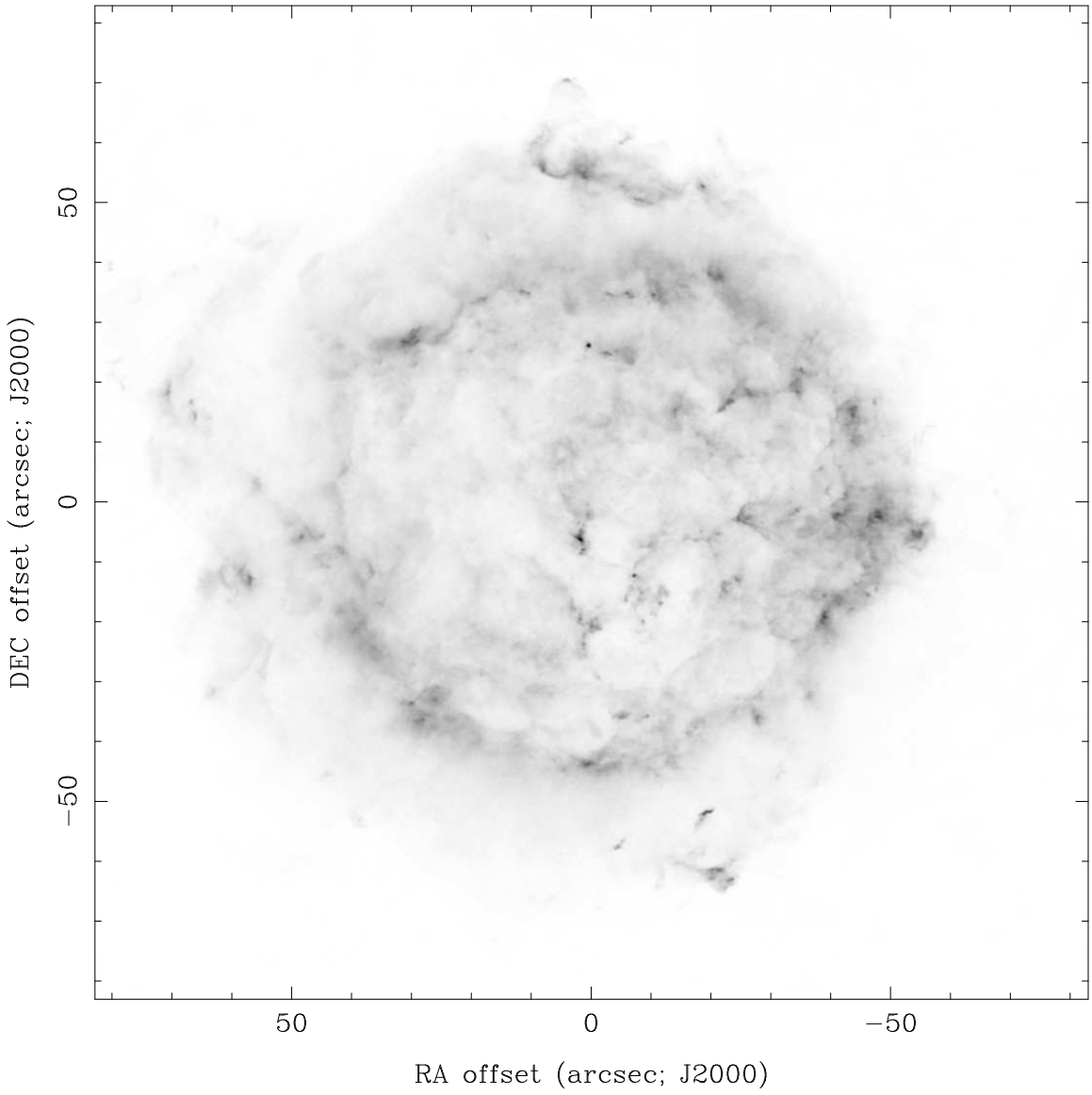

Fig. 1.— VLA Image model of Cas A scaled to 128″ diameter

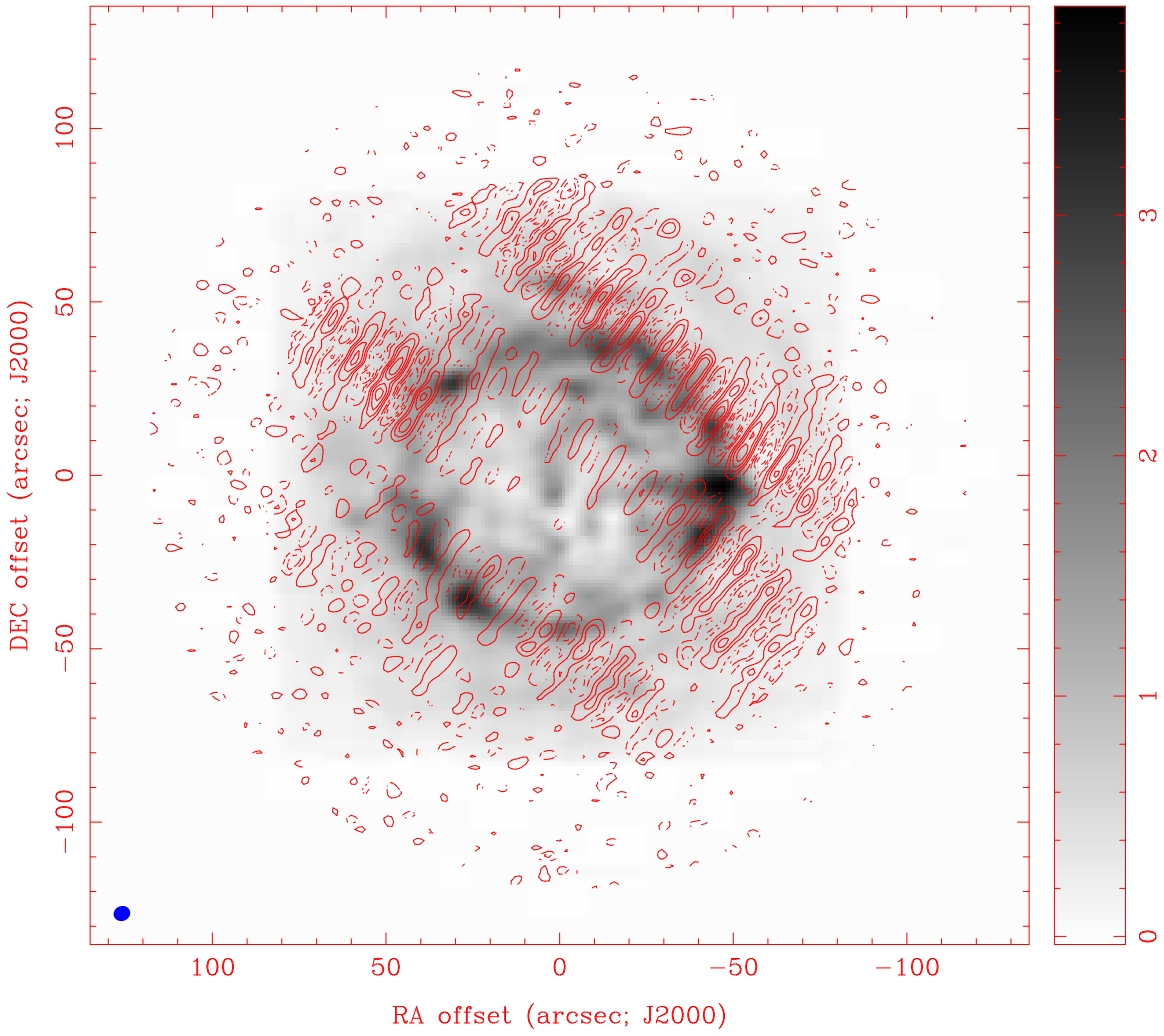

Fig. 2.— Mosaic Image of Cas A model scaled to 128″ diameter observed with the CARMA 15-antenna D configuration using a single pointing center at an observing frequency 100 GHz. The grey scale pixel image shows the maximum entropy deconvolution using the three standard truncated Gaussian primary beam models for 10m-10m 10m-6m and 6m-6m antenna pairs. The contours show the residual image when the measured voltage patterns for just one antenna pair, antennas 1 and 8, is used instead of the truncated Gaussian model. Contour intervals: -.004, -.003, -.002, -.001, .001, .002, .003, .004 Jy.

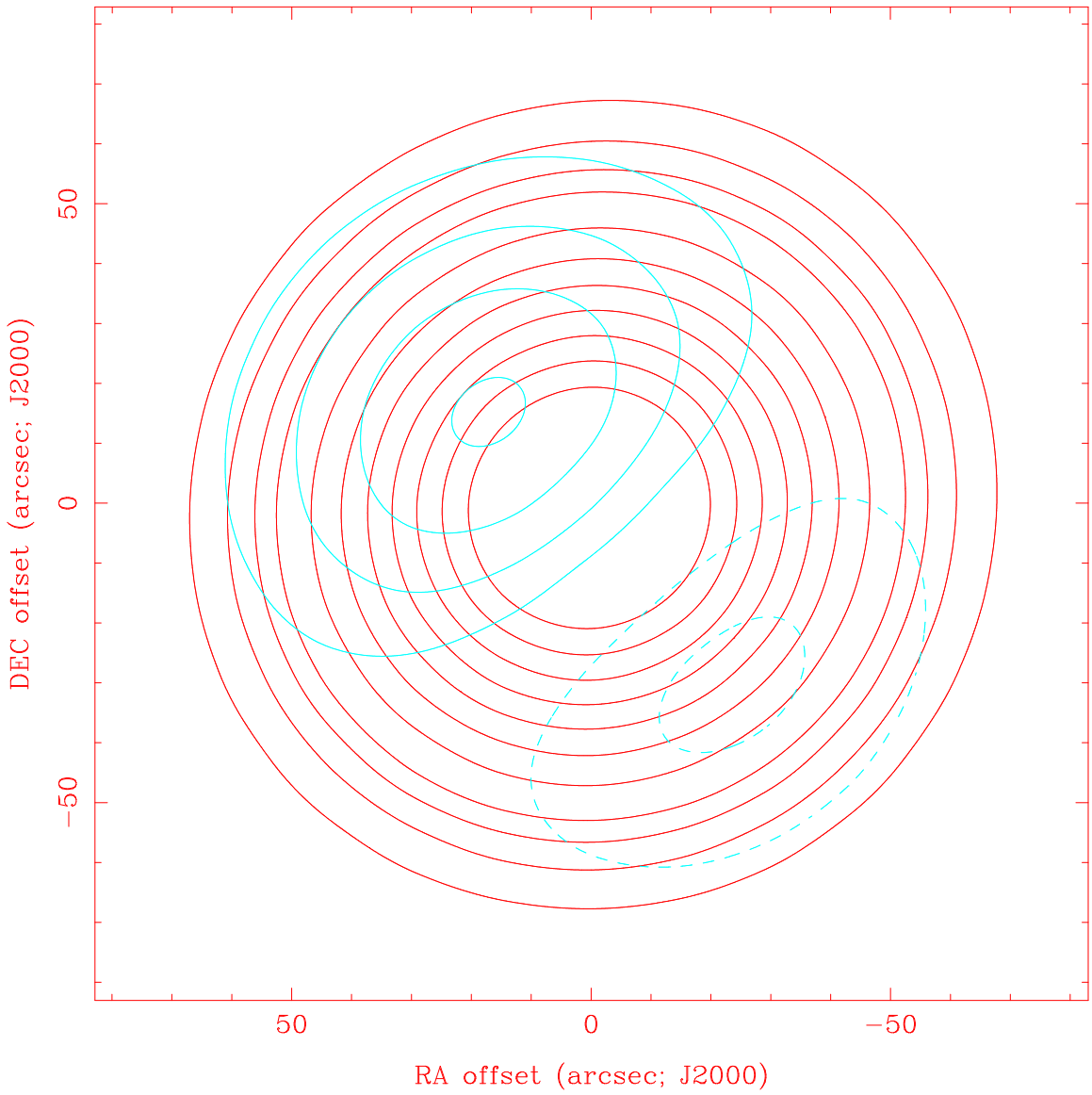

Fig. 3.— Primary beam pattern for cross correlation between two 10m antennas: 2 and 6. The red contours are the real part of the primary beam response. The blue contours are the imaginary part of the primary beam response. contour levels=-.2,-.15,-.1,-.05,.05,.10,.15,.2,.3,.4,.5,.6,.7,.8,.9

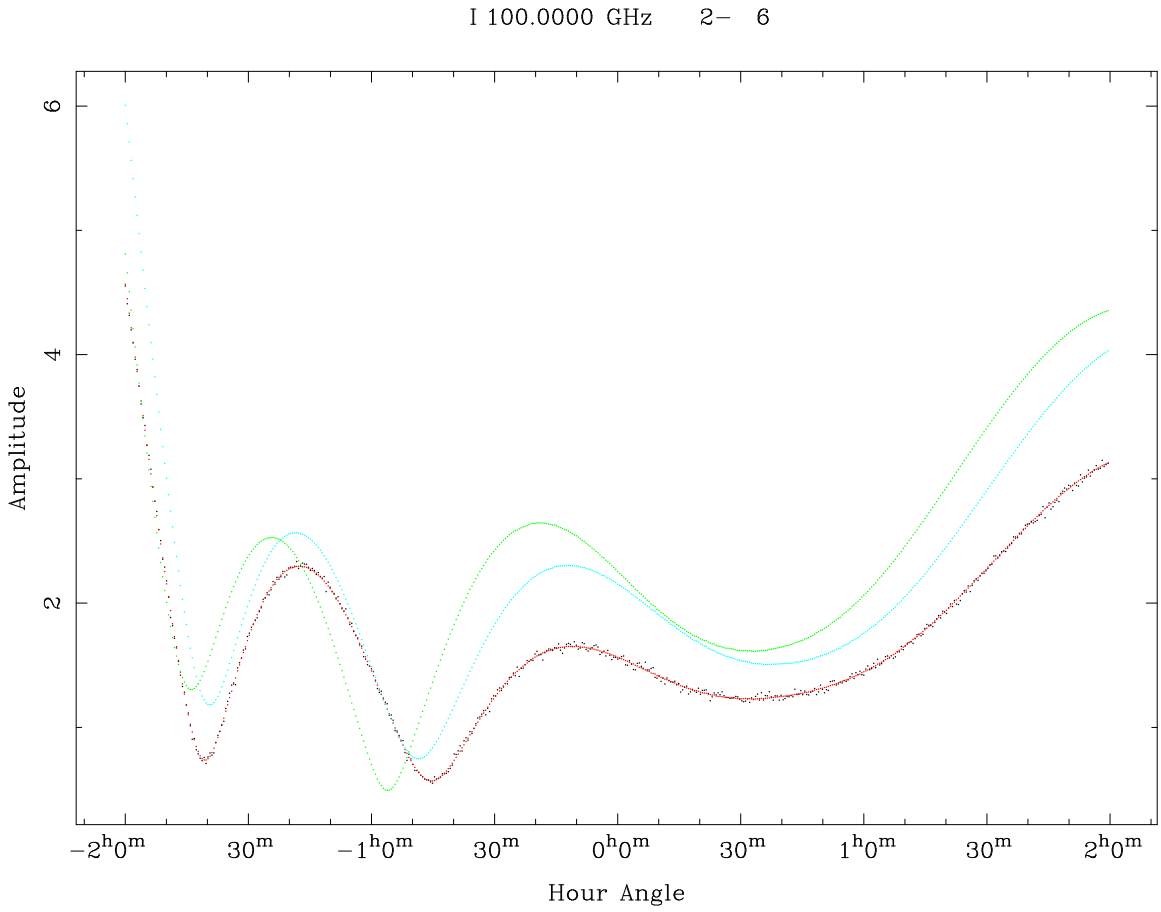

Fig. 4.— Amplitude of *uv* data from a central pointing with antennas 2 and 6. Black points are the simulated *uv* data. The red curve is the model visibility for the Gaussian model primary beam pattern used to generate the *uv* data. The blue curve is the model visibility using the real part of the measured primary beam response. The green curve is the model visibility using the real and imaginary parts of the measured primary beam response.

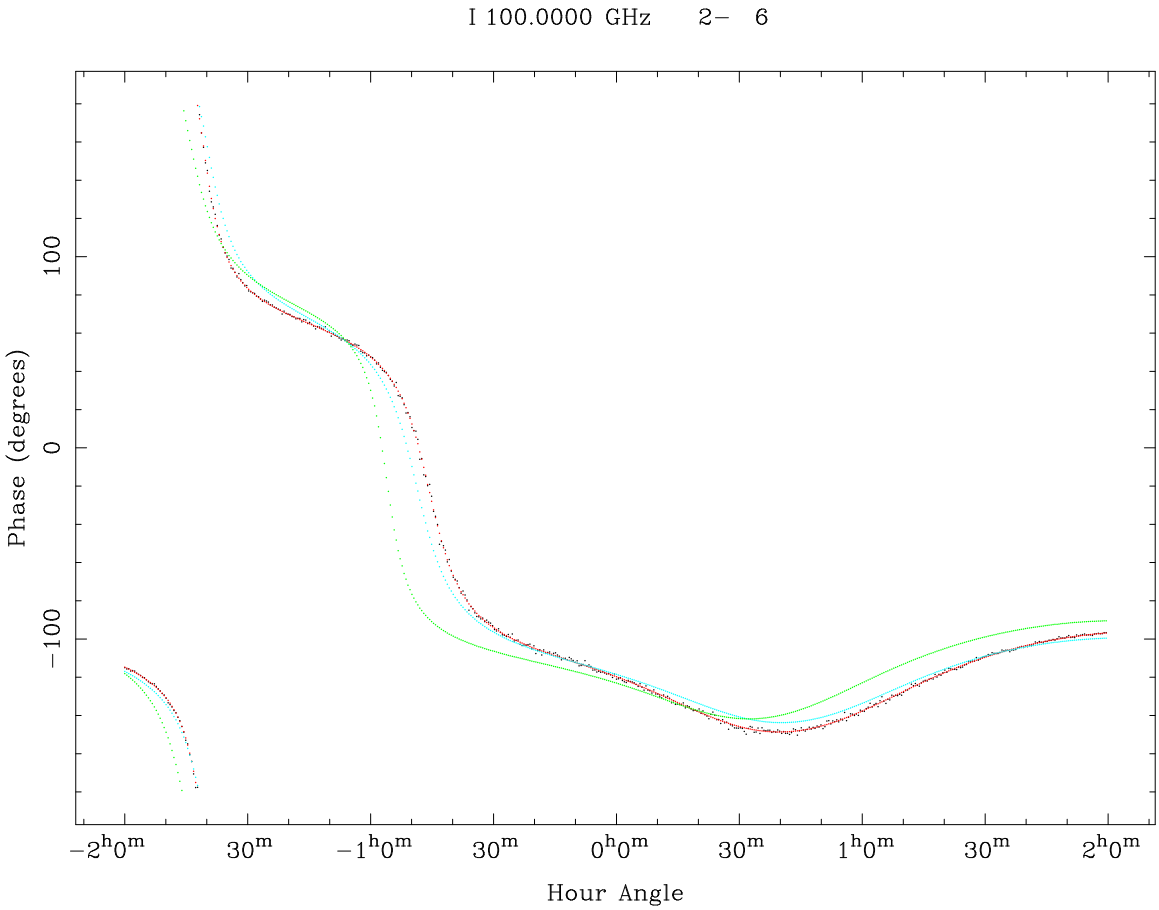

Fig. 5.— Phase of *uv* data from a central pointing with antennas 2 and 6. Black points are the simulated *uv* data. The red curve is the model visibility for the Gaussian model primary beam pattern used to generate the *uv* data. The blue curve is the model visibility using the real part of the measured primary beam response. The green curve is the model visibility using the real and imaginary parts of the measured primary beam response.

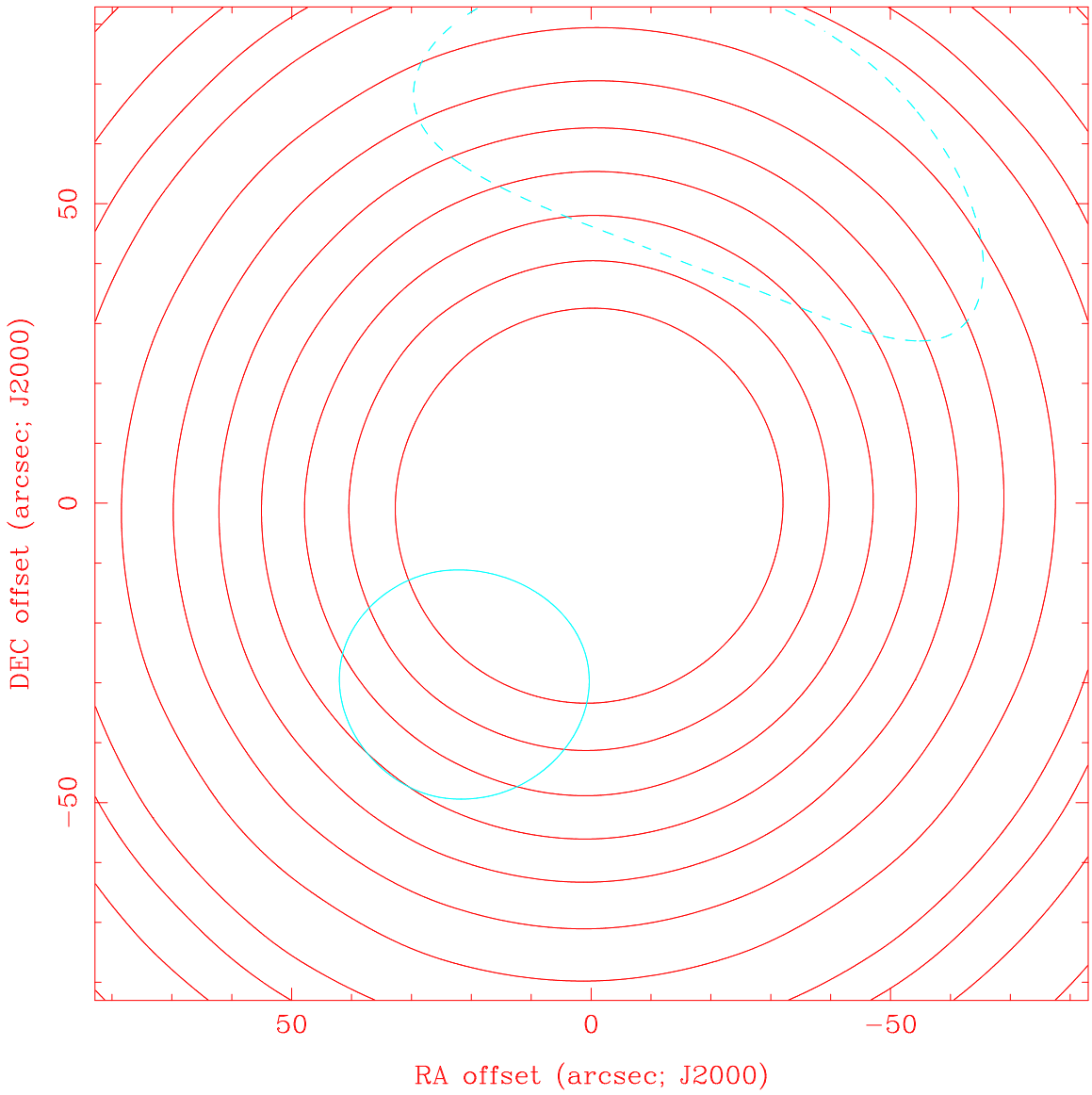

Fig. 6.— Primary beam pattern for cross correlation between two 6m antennas: 7 and 9. The red contours are the real part of the primary beam response. The blue contours are the imaginary part of the primary beam response. contour levels=-.2,-.15,-.1,-.05,.05,.10,.15,.2,.3,.4,.5,.6,.7,.8,.9

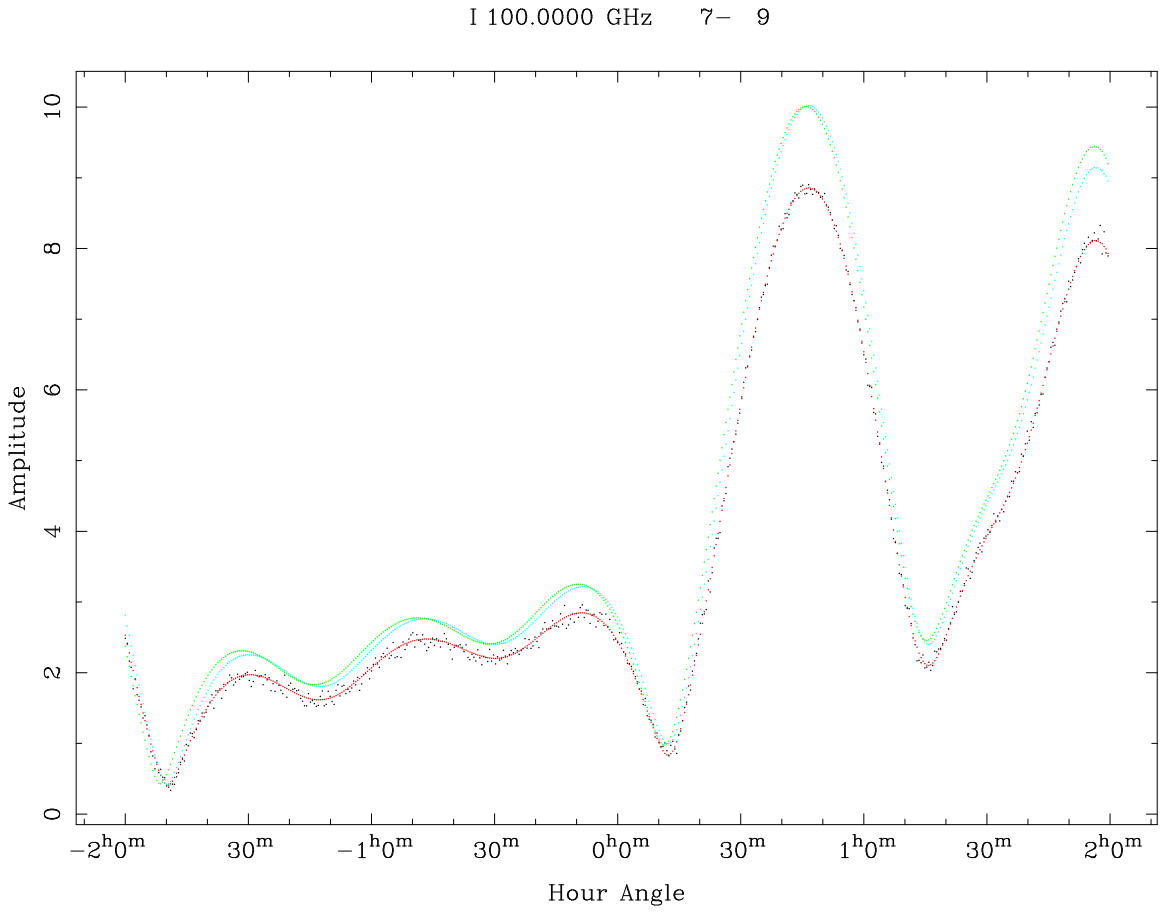

Fig. 7.— Amplitude of *uv* data from a central pointing with antennas 7 and 9. Black points are the simulated *uv* data. The red curve is the model visibility for the Gaussian model primary beam pattern used to generate the *uv* data. The blue curve is the model visibility using the real part of the measured primary beam response. The green curve is the model visibility using the real and imaginary parts of the measured primary beam response.

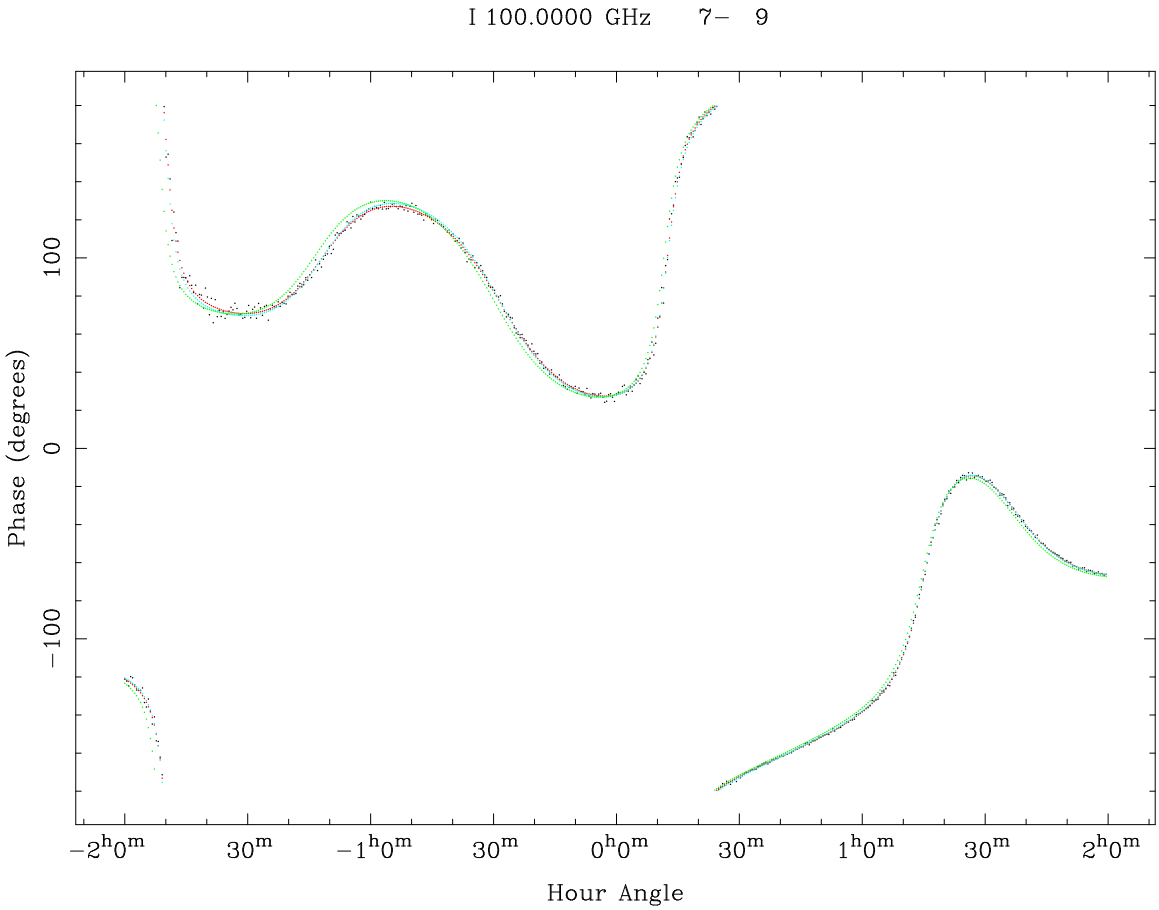

Fig. 8.— Phase of *uv* data from a central pointing with antennas 7 and 9. Black points are the simulated *uv* data. The red curve is the model visibility for the Gaussian model primary beam pattern used to generate the *uv* data. The blue curve is the model visibility using the real part of the measured primary beam response. The green curve is the model visibility using the real and imaginary parts of the measured primary beam response.

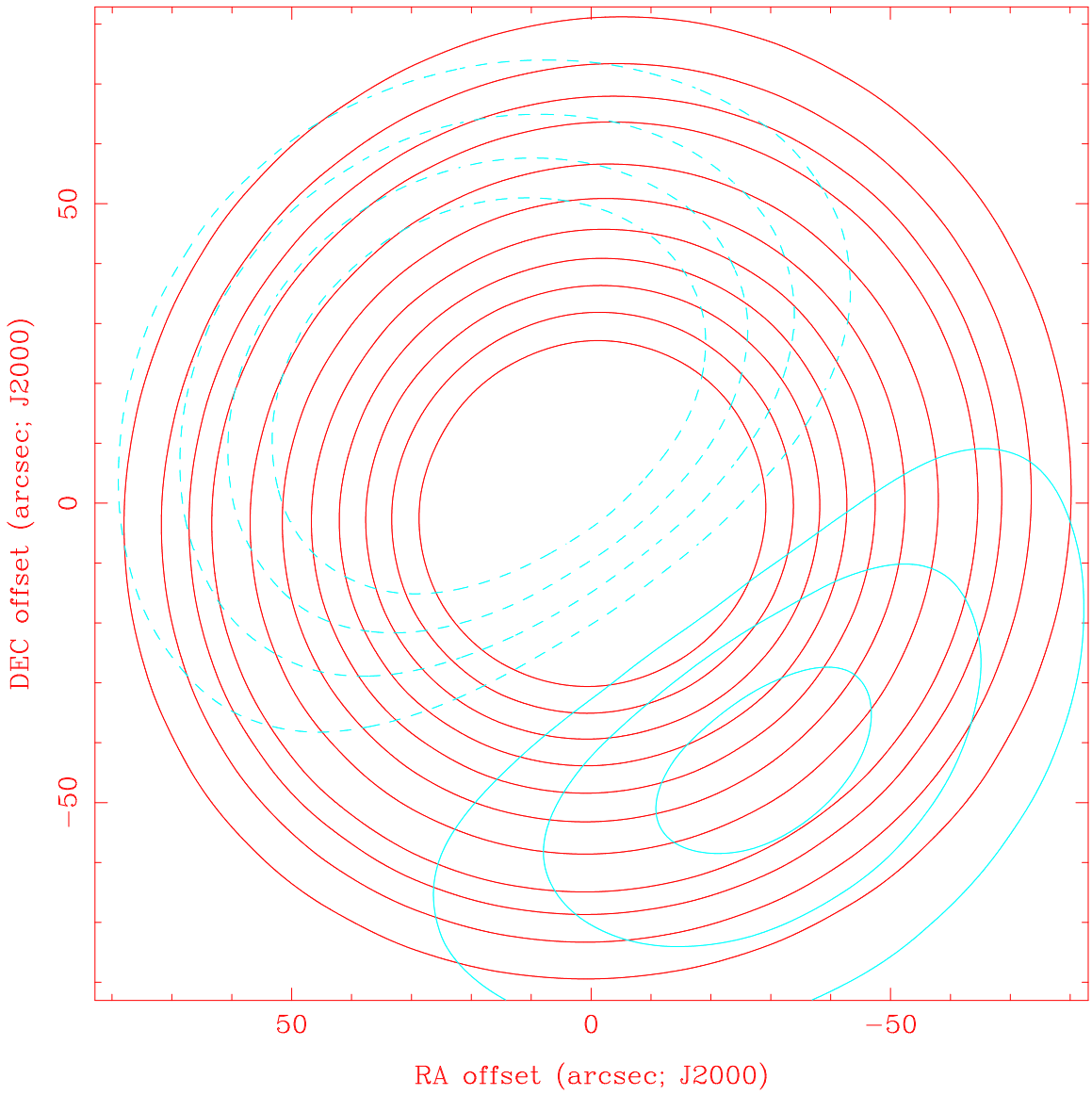

Fig. 9.— Primary beam pattern for cross correlation between 10m and 6m antennas: 6 and 11. The red contours are the real part of the primary beam response. The blue contours are the imaginary part of the primary beam response. contour levels=-.2,-.15,-.1,-.05,.05,.10,.15,.2,.3,.4,.5,.6,.7,.8,.9

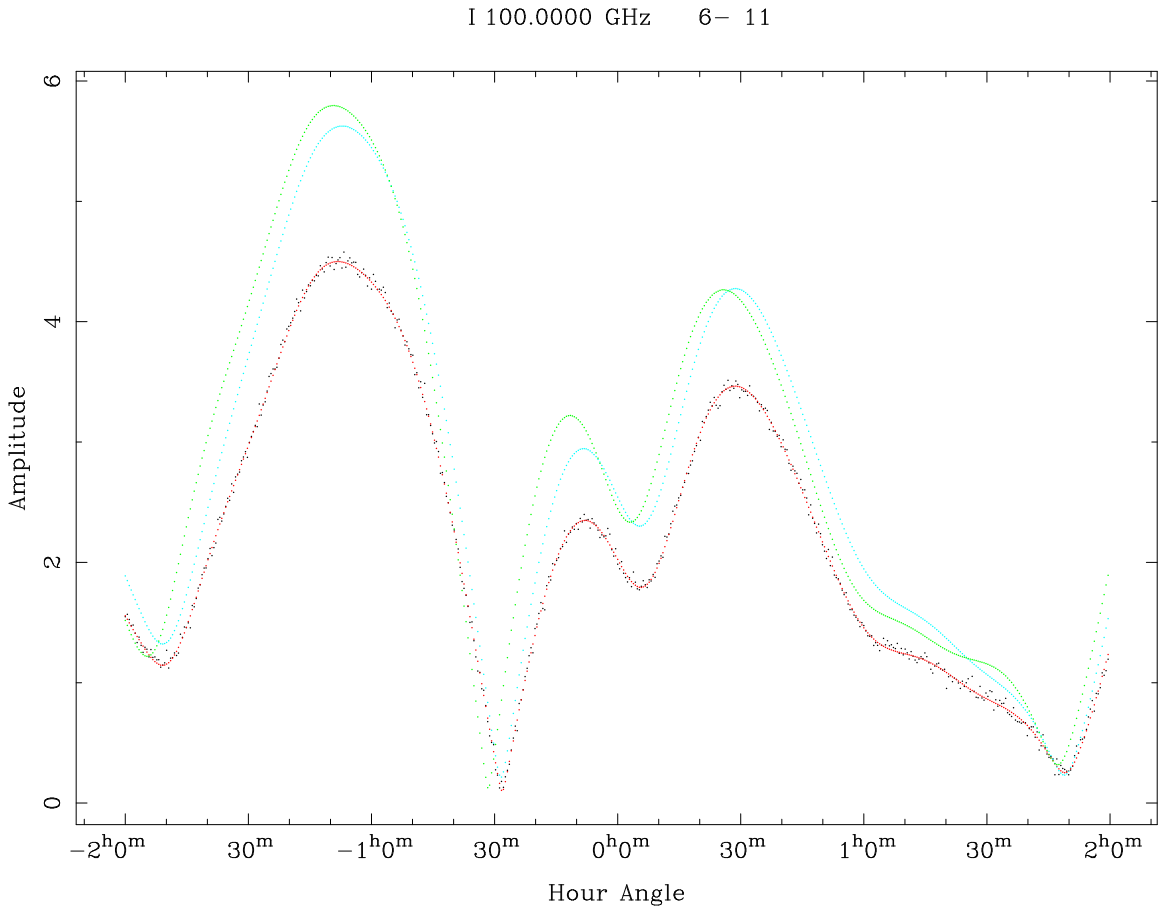

Fig. 10.— Amplitude of *uv* data from a central pointing with antennas 6 and 11. Black points are the simulated *uv* data. The red curve is the model visibility for the Gaussian model primary beam pattern used to generate the *uv* data. The blue curve is the model visibility using the real part of the measured primary beam response. The green curve is the model visibility using the real and imaginary parts of the measured primary beam response.

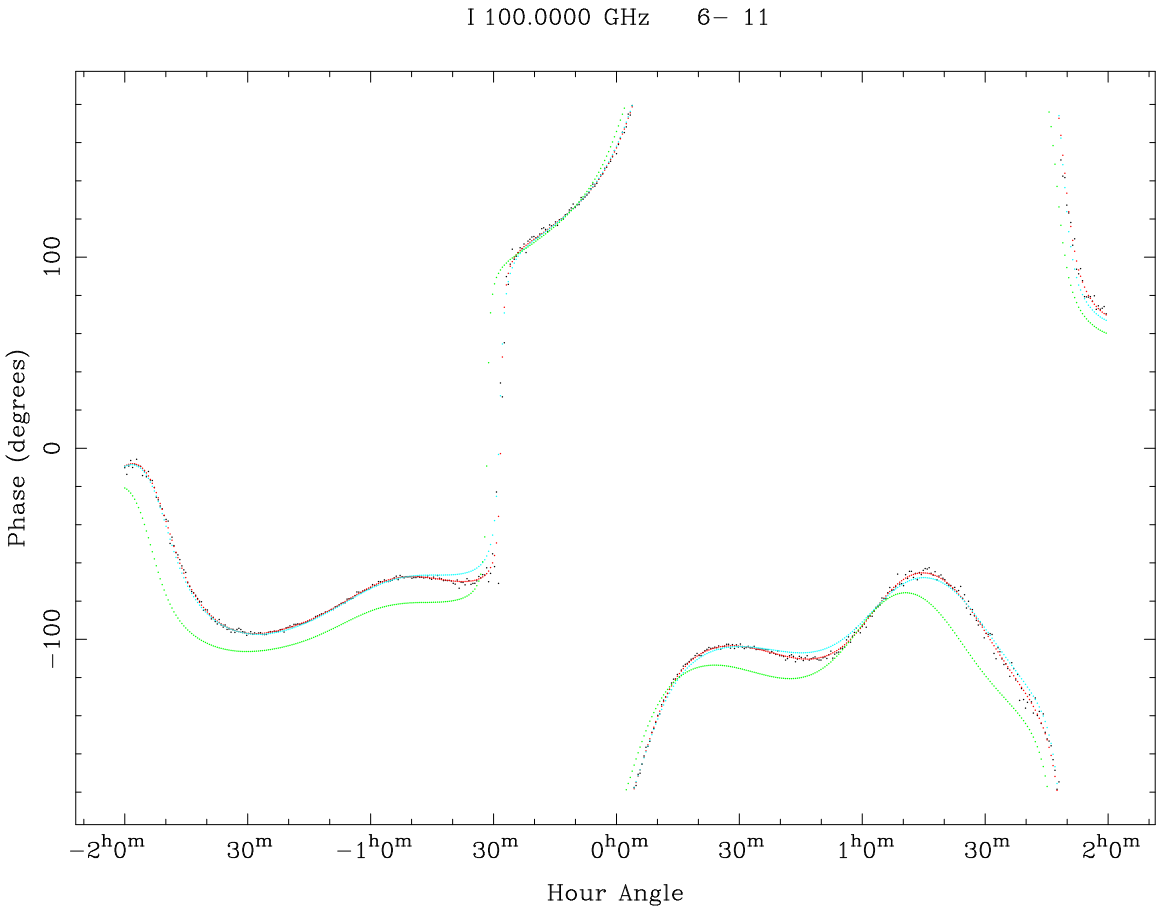

Fig. 11.— Phase of *uv* data from a central pointing with antennas 6 and 11. Black points are the simulated *uv* data. The red curve is the model visibility for the Gaussian model primary beam pattern used to generate the *uv* data. The blue curve is the model visibility using the real part of the measured primary beam response. The green curve is the model visibility using the real and imaginary parts of the measured primary beam response.

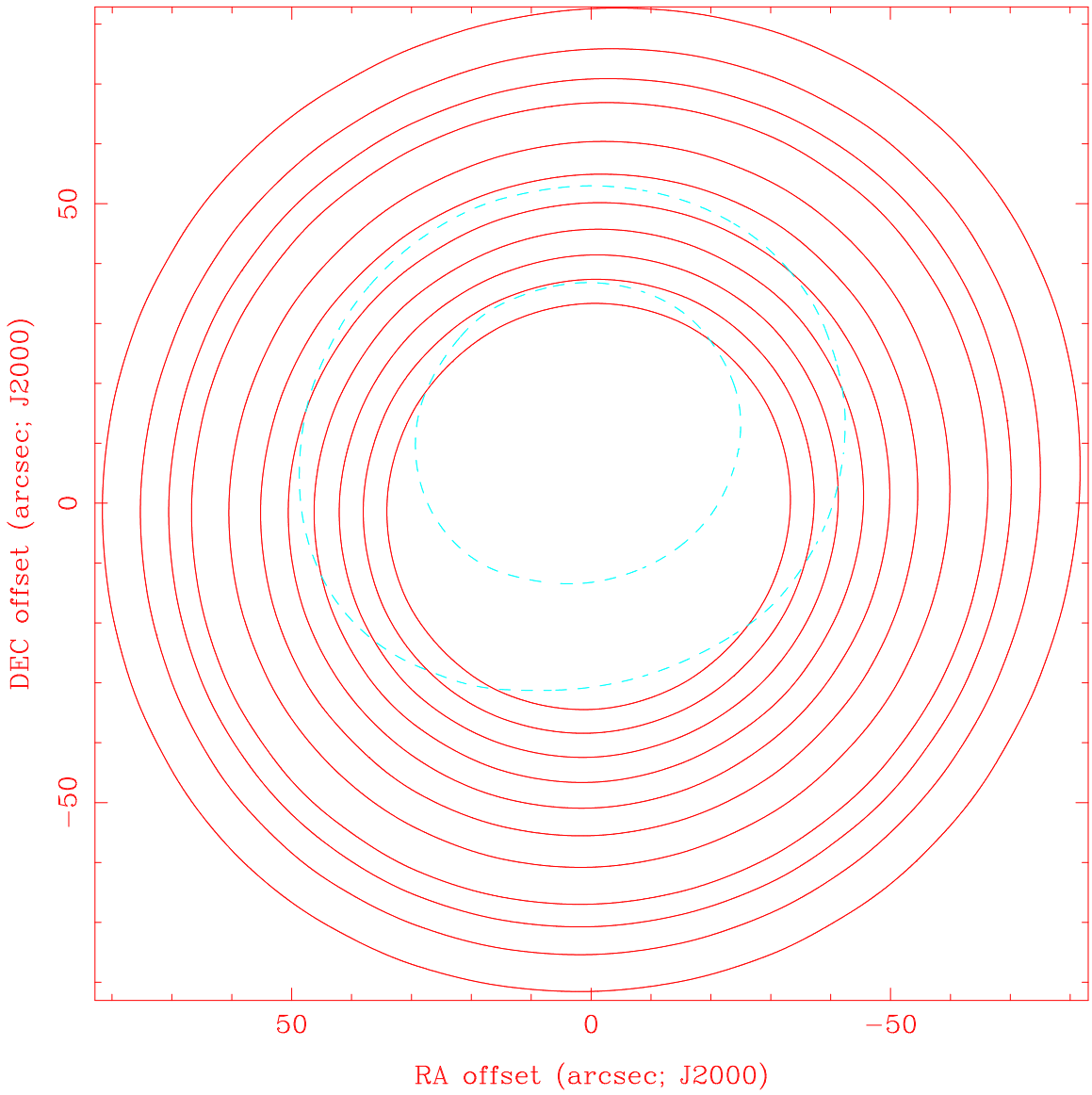

Fig. 12.— Primary beam pattern for cross correlation between 10m and 6m antennas: 2 and 11. The red contours are the real part of the primary beam response. The blue contours are the imaginary part of the primary beam response. contour levels=-.2,-.15,-.1,-.05,.05,.10,.15,.2,.3,.4,.5,.6,.7,.8,.9

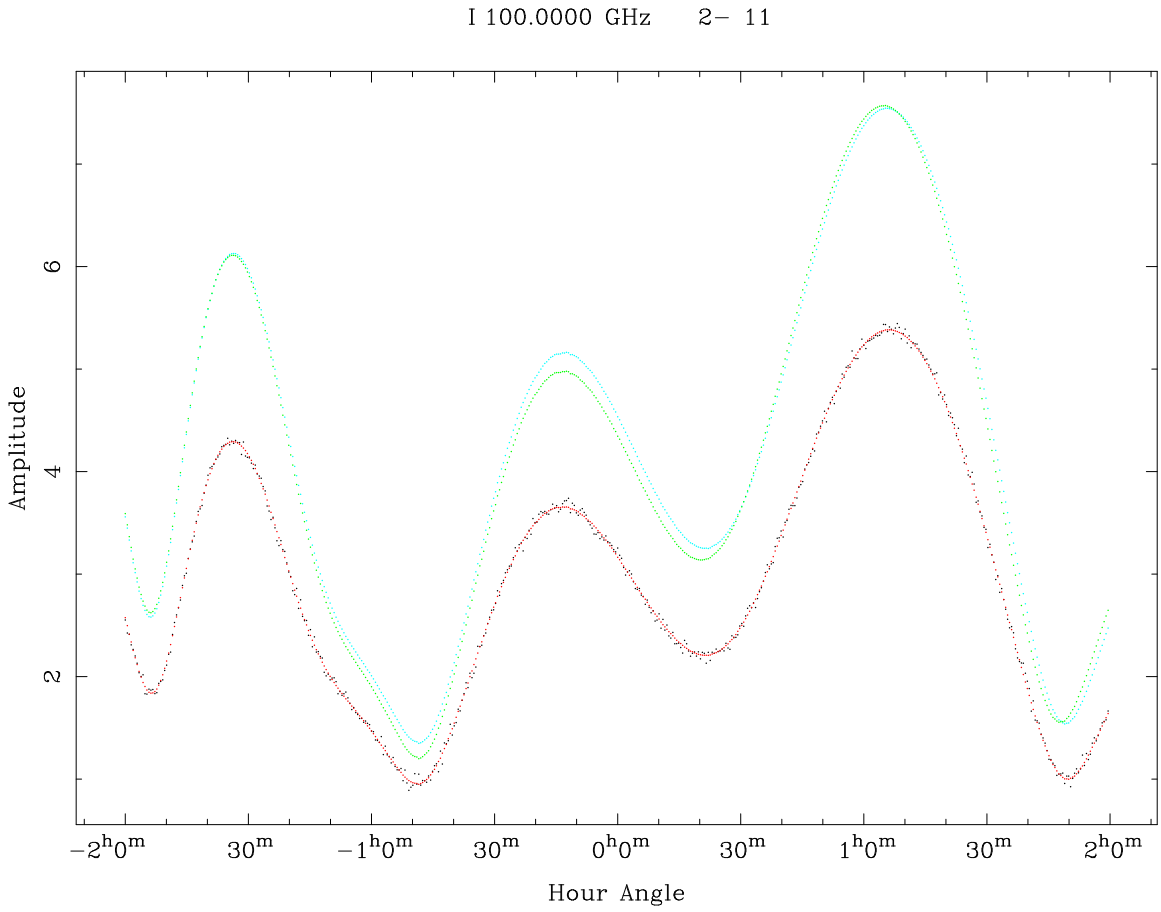

Fig. 13.— Amplitude of *uv* data from a central pointing with antennas 2 and 11. Black points are the simulated *uv* data. The red curve is the model visibility for the Gaussian model primary beam pattern used to generate the *uv* data. The blue curve is the model visibility using the real part of the measured primary beam response. The green curve is the model visibility using the real and imaginary parts of the measured primary beam response.

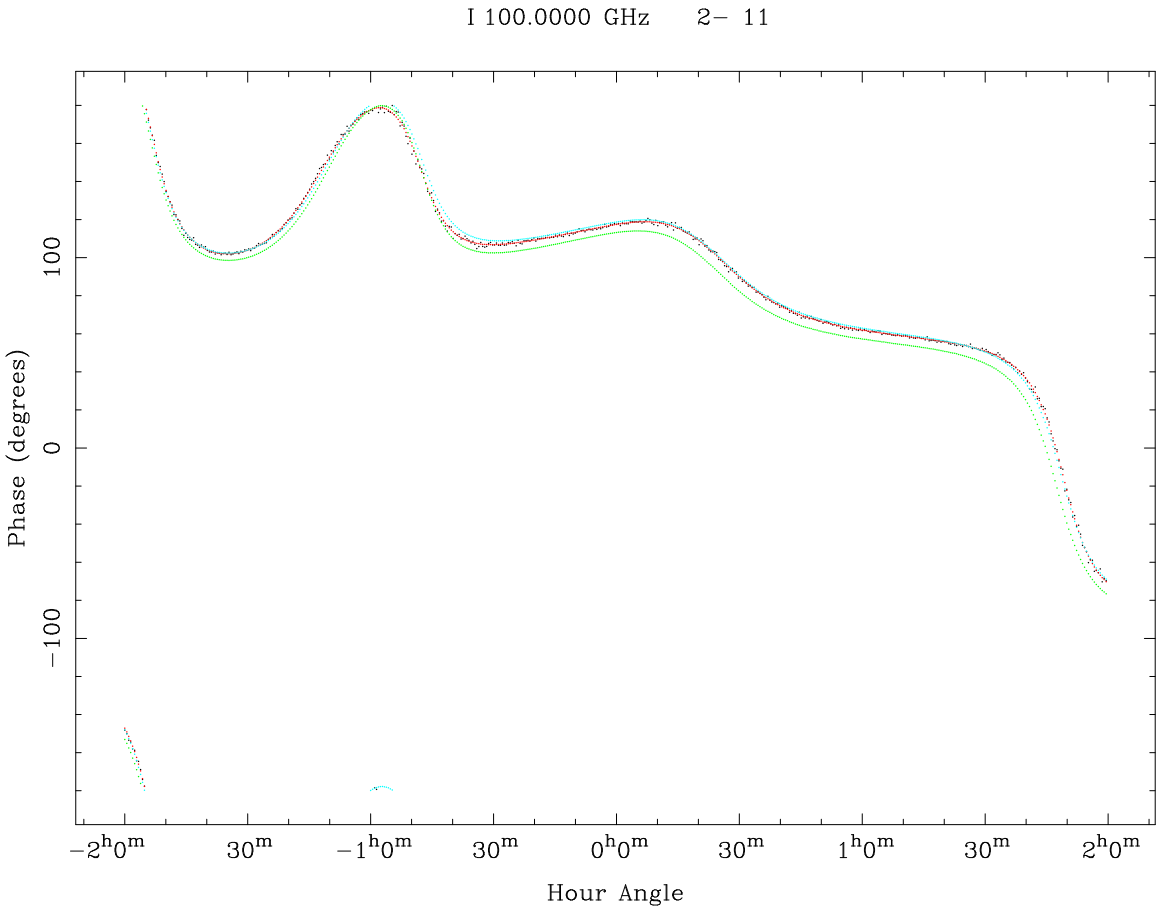

Fig. 14.— Phase of *uv* data from a central pointing with antennas 2 and 11. Black points are the simulated *uv* data. The red curve is the model visibility for the Gaussian model primary beam pattern used to generate the *uv* data. The blue curve is the model visibility using the real part of the measured primary beam response. The green curve is the model visibility using the real and imaginary parts of the measured primary beam response.

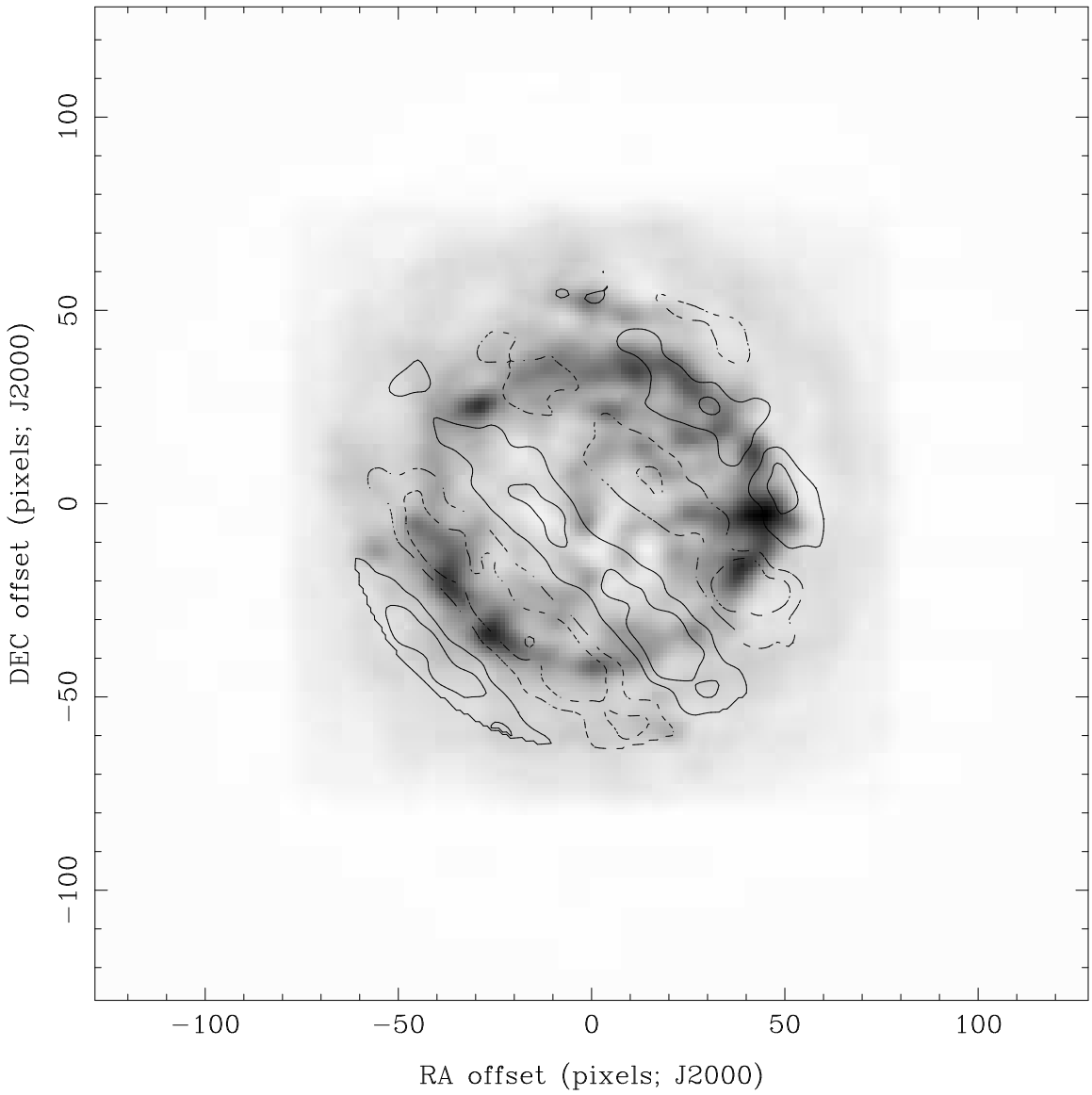

Fig. 15.— Instrumental polarization response across the primary beam. Mosaic Image of Cas A model scaled to 128″ diameter observed with the CARMA 15-antenna D configuration using a single pointing center at an observing frequency 100 GHz. The grey scale pixel image shows the maximum entropy deconvolution using the three standard truncated Gaussian primary beam models for 10m-10m 10m-6m and 6m-6m antenna pairs. The contours show the imaginary part of the image when the measured voltage patterns for all antenna pairs are used instead of the truncated Gaussian model. The *uv* data were sampled from -2 to +2 hours with the primary beam rotated to the correct paralactic angle at 0.5 hour intervals. Contour intervals at 5, 10 and 20% of the peak in the total intensity image.

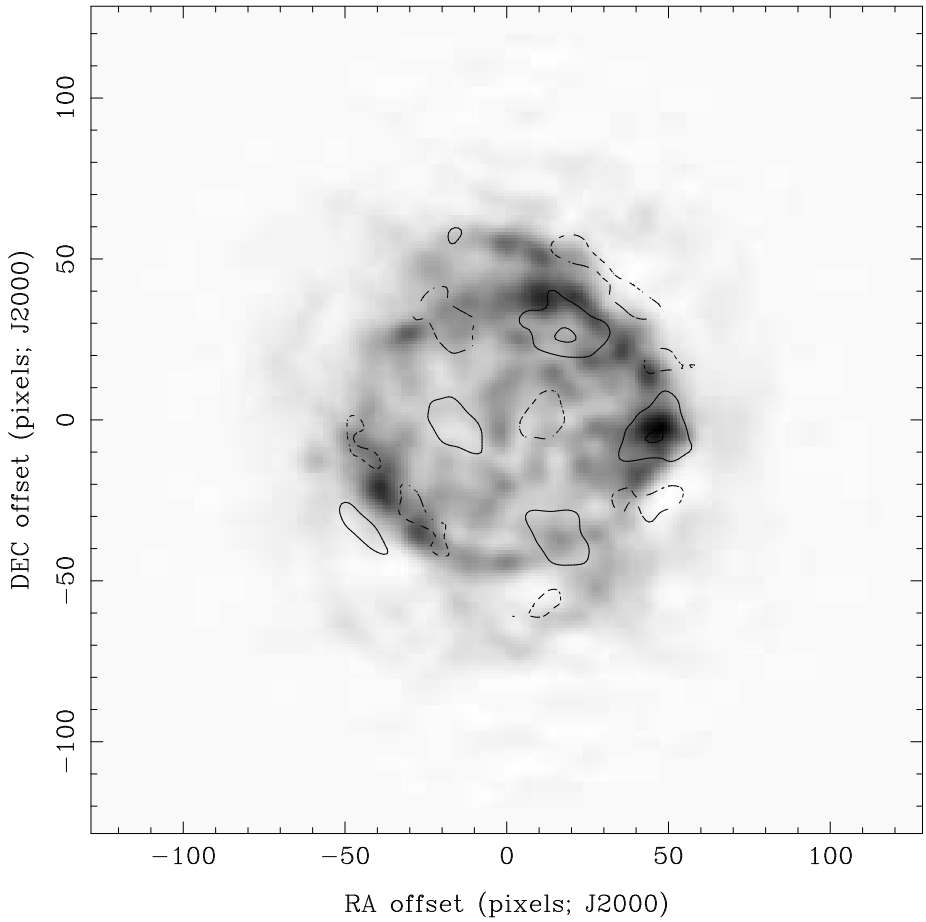

RA, DEC, VELO = 12:00:00.000, 30:00:00.00, 0.00000E+00 km/s at pixel (129.00, 129.00, 1.00)
Spatial region : 1,1 to 257,257
Pixel map image: casc.vla.temp.cm (ovro.ha0.uv) Min/max=−0.1225/4.945 Range = −0.1225 to 4.945 JY/BEAM (lin)
Contour image: casc.vla.temp.imaginary.fixedC1.map (ovro.ha0.uv) Min/max=−0.4243/0.5257 JY/BEAM
Contours : −0.98, −0.49, −0.245, 0.245, 0.49, 0.98

Fig. 16.— Instrumental polarization response across the primary beam is significantly improved by reducing the imaginary part of the primary beam response which arises from asymmetries in the aperture illumination. In this figure, the voltage pattern for antenna 1 is corrected to the errors measured in antenna 3. Mosaic Image of Cas A model scaled to 128″ diameter observed with the CARMA 15-antenna D configuration using a single pointing center at an observing frequency 100 GHz. The grey scale pixel image shows the maximum entropy deconvolution using the three standard truncated Gaussian primary beam models for 10m-10m 10m-6m and 6m-6m antenna pairs. The contours show the imaginary part of the image when the measured voltage patterns for all antenna pairs are used instead of the truncated Gaussian model. The *uv* data were sampled from -2 to +2 hours with the primary beam rotated to the correct paralactic angle at 0.5 hour intervals. Contour intervals at 5, 10 and 20% of the peak in the total intensity image.